ROYAL SOCIETY
OF CHEMISTRY

PAPER

Check for updates

Dual-emission ratiometric fluorescent sensor based on tannic acid carbon dots and eosin for selective detection of paraquat in water and food samples

Mohamed N. Goda,[a] Laila S. Alqarni,[a] K. S. Al-Namshah,[a] Faisal K. Algethami,[a] Hossieny Ibrahim,[b] Mohamed M. El-Wekil [iD][c] and Al-Montaser Bellah H. Ali [iD] *[c]

Paraquat, a highly toxic herbicide widely used in agriculture, poses severe health risks necessitating sensitive analytical methods for residue monitoring in environmental and food samples. This work presents a novel dual-emission ratiometric fluorescent sensor combining tannic acid-derived carbon dots (TA-CDs) and eosin for rapid paraquat detection. The dicationic paraquat simultaneously induces aggregation-enhanced fluorescence of TA-CDs at 445 nm while quenching eosin emission at 545 nm, generating a self-calibrated ratiometric signal (F_{445}/F_{545}). The TA-CDs were comprehensively characterized using TEM, Raman, FTIR, XPS, and spectroscopic techniques. Under optimized conditions, the sensor exhibited excellent linearity (5.0–150.0 nM, $R^2 = 0.9973$) with a detection limit of 2.11 nM. The mechanism was validated through spectral overlap analysis, zeta potential measurements, and TEM imaging. Exceptional selectivity was demonstrated against common interferants due to the unique dual-recognition requirement. The method achieved excellent recoveries of 96.4% to 98.2% in Nile River water and 96.9% to 99.6% in cabbage extracts. Application to agricultural cabbage samples at different days post-application revealed decreasing paraquat residues from above to below the maximum residue limit, demonstrating practical capability for food safety monitoring. This metal-free, cost-effective platform offers rapid response and simplified operation for routine paraquat surveillance in environmental and agricultural systems.

1. Introduction

Paraquat (1,1′-dimethyl-4,4′-bipyridinium dichloride) is a highly effective non-selective contact herbicide widely used in agriculture for weed control in various crops, plantation settings, and non-crop areas.[1] However, its widespread use has raised significant concerns regarding human health and environmental safety.[2–4] Paraquat is highly toxic to humans, with acute exposure potentially causing severe damage to multiple organs, particularly the lungs, liver, and kidneys, while chronic exposure has been linked to neurological disorders including Parkinson's disease.[5–7] Environmentally, paraquat poses risks to non-target organisms, soil microbiota, and aquatic ecosystems through runoff and persistence in various environmental compartments. Due to these hazards, many countries have established strict maximum residue limits (MRLs) for paraquat in food commodities, typically ranging from 0.01 to 0.5 mg kg^{-1} depending on the crop type, while occupational exposure limits

are set at approximately 0.1 mg m^{-3} for air and 0.005 mg L^{-1} for drinking water according to WHO guidelines.[8] The determination and monitoring of paraquat residues in diverse matrices including agricultural products, water, soil, and biological samples is therefore of paramount importance for regulatory compliance, food safety assessment, environmental protection, and public health surveillance, necessitating the development of sensitive, selective, and reliable analytical methods.

Most established paraquat assays carry practical drawbacks. HPLC/LC-MS offers gold-standard selectivity but often needs ion-pairing or derivatization, intensive clean-up, skilled operators, and expensive instruments—slowing turnaround and raising costs.[9–11] Electrochemical sensors are portable yet prone to electrode fouling, baseline drift, and redox interferents.[12–14] Colorimetric tests are simple but frequently lack ppb sensitivity and are susceptible to matrix color/turbidity.[15,16] SERS/other optical schemes can be ultra-sensitive, but they depend on specialty substrates, careful aggregation control, and chemometric modeling,[17] which complicate reproducibility and field deployment. Immunoassays reduce hardware needs but may suffer cross-reactivity and reagent instability.[18]

By contrast, fluorometric methods (*e.g.*, carbon-dot or reaction-based probes) provide nM-level sensitivity, minutes-scale assays, and simple, low-cost optics.[19–23] Chemistry can be

[a]Department of Chemistry, College of Science, Imam Mohammad Ibn Saud Islamic University (IMSIU), Riyadh 11623, Saudi Arabia

[b]School of Biotechnology, Badr University in Assiut, Assiut 2014101, Egypt

[c]Department of Pharmaceutical Analytical Chemistry, Faculty of Pharmacy, Assiut University, Assiut, Egypt. E-mail: Almontaser_bellah@aun.edu.eg

engineered for intrinsic selectivity (*e.g.*, reaction-based recognition) or ratiometric/lifetime readouts that suppress intensity drift, inner-filter, and background issues in colored extracts. They work with small sample volumes, minimal pretreatment, and translate readily to microplate or handheld formats for on-site screening.[24–27] With appropriate controls (spike-recovery, matrix-matched calibration) and a brief selectivity panel including structure related pesticides and common ions/metals, fluorometric assays offer a practical balance of sensitivity, specificity, and portability for routine paraquat monitoring.[28,29]

Carbon dots (CDs), also known as carbon quantum dots or carbon nanodots, have emerged as a promising class of fluorescent nanomaterials for analytical applications, particularly in pesticide detection.[30] These quasi-spherical nanoparticles, typically less than 10 nm in diameter, exhibit exceptional photoluminescent properties, including tunable emission wavelengths, high quantum yields, photostability, and resistance to photobleaching.[31,32] CDs can be synthesized through simple, cost-effective, and environmentally friendly methods using various carbon-rich precursors, including biomass, organic compounds, and even agricultural waste, making them attractive alternatives to conventional semiconductor quantum dots and organic fluorophores.[33] Their unique optical properties, combined with abundant surface functional groups (hydroxyl, carboxyl, and amino groups), enable versatile surface modification and functionalization strategies for selective molecular recognition.[34] In the context of pesticide detection, CDs have demonstrated remarkable sensitivity and selectivity through various sensing mechanisms, including fluorescence quenching or enhancement, fluorescence resonance energy transfer (FRET), and inner filter effects.[35] CDs-based fluorescent probes have been successfully applied for detecting various pesticide classes including organophosphates, carbamates, neonicotinoids, and bipyridinium herbicides like paraquat in complex matrices such as food products, water samples, and soil extracts.[36–38] The advantages of CD-based sensors include rapid response times, low detection limits (often at ppb or sub-ppb levels), minimal sample preparation, potential for on-site and real-time monitoring, biocompatibility, and low toxicity, positioning them as powerful tools for ensuring food safety and environmental monitoring in the context of pesticide contamination.[39]

The novelty of this work lies in the development of an innovative dual-emission ratiometric fluorescent sensing platform for paraquat detection, combining tannic acid derived carbon dots (TA-CDs) and eosin. Unlike conventional single-emission fluorescent sensors that are susceptible to environmental interferences and instrumental fluctuations, the proposed ratiometric system offers significant advantages through self-calibration and enhanced reliability. The unique sensing mechanism is based on the differential response of the two fluorophores to paraquat: upon addition of the target analyte, the fluorescence emission of eosin at 545 nm is quenched, while simultaneously, the fluorescence emission of TA-CDs at 445 nm is enhanced. This opposite and concurrent change in the two emission signals enables ratiometric detection with

improved accuracy, sensitivity, and resistance to background interference. The dual-signal response mechanism eliminates false-positive results and compensates for external factors such as photobleaching, pH variations, and matrix effects, which commonly plague single-emission sensors. The practical applicability of this novel sensing platform has been successfully demonstrated for paraquat determination in vegetables and environmental samples, offering a rapid, sensitive, and reliable analytical tool for food safety monitoring and environmental surveillance without requiring sophisticated instrumentation or complex sample pretreatment procedures.

Regarding the selection of tannic acid-derived carbon dots and eosin, the design was theoretically deduced based on rational complementary criteria: (a) we identified TA-CDs from literature exhibiting aggregation-induced emission enhancement at ~445 nm with excitation at 335 nm—a desirable property for positive ratiometric response;[40] (b) eosin was selected as it can be co-excited at the same wavelength (335 nm) while emitting at a distinct wavelength (545 nm), providing spectral separation; and (c) both components possess negative charges conducive to electrostatic interaction with dicationic paraquat, enabling dual opposite responses (TA-CD enhancement *via* aggregation and eosin quenching *via* binding).

2. Experimental

2.1. Materials and reagents

Paraquat dichloride, dichlorvos (DDVP), glyphosate, atrazine, pendimethalin, fluroxypyr, propisochlor, quizalofop, tribenuron-methyl, acetochlor, MCPA-Na, metolachlor, tebuconazole, eosin Y, tannic acid, and humic acid were purchased from Sigma-Aldrich (St. Louis, MO, USA). Citric acid, urea, sodium chloride (NaCl), potassium chloride (KCl), calcium chloride ($CaCl_2$), magnesium chloride ($MgCl_2$), ammonium chloride (NH_4Cl), sodium nitrate ($NaNO_3$), and sodium sulfate (Na_2SO_4) were obtained from Merck (Darmstadt, Germany). Sodium bicarbonate ($NaHCO_3$), trisodium phosphate (Na_3PO_4), ferrous sulfate ($FeSO_4$), copper(II) sulfate ($CuSO_4$), and zinc sulfate ($ZnSO_4$) were supplied by Alpha Chemika Co., India. Nickel(II) sulfate ($NiSO_4$), lead(II) nitrate [$Pb(NO_3)_2$], mercury(II) chloride ($HgCl_2$), and aluminum chloride ($AlCl_3$) were purchased from El-Naser Co. Cario, Egypt. All stock and working solutions were prepared with ultrapure water (18.2 MΩ cm) and stored in acid-washed polyethylene bottles.

2.2. Instrumentation and characterization

Please refer to the accompanying SI for the full instrumentation details.

2.3. Synthesis of TA-CDs

Tannic acid-derived carbon dots were synthesized *via* a facile one-step previously reported hydrothermal method with slight modification.[40] Under continuous magnetic agitation, tannic acid (1.0 g) was fully solubilized in ultra-pure water (40 mL). The aqueous mixture was placed in a Teflon-lined stainless–steel reaction vessel (50 mL capacity), tightly closed, and

subjected to hydrothermal treatment at 160 °C for a duration of 4 hours. Following spontaneous temperature reduction to ambient conditions, the brown-colored product underwent centrifugal separation at 10 000 rpm for 15 minutes. The liquid phase was recovered and purified through dialysis tubing (1000 Da molecular weight cutoff) against ultra-pure water over 24 hours, replacing the external water every 6 hours. The refined TA-CDs dispersion was then reduced in volume *via* rotary evaporation and preserved at 4 °C until required for experiments.

2.4. Quantum yield of the prepared TA-CDs

Details of the quantum-yield calculation are provided in the SI file.

2.5. Procedure for detection of paraquat

For paraquat detection, a dual-emission sensing system was constructed using eosin and the TA-CDs. In a typical analysis, 500 μL of TA-CDs solution (1.0 mg mL^{-1}), 200 μL of eosin solution (0.1 0.01 mg mL^{-1}), and 200 μL of phosphate buffer (50 mM, pH 8.0) were mixed in a quartz cuvette. Various concentrations of paraquat standard or sample solutions (100 μL) were then added, and the mixture was diluted to a final volume of 3.0 mL with ultra-pure water. The solution was thoroughly mixed and incubated at room temperature for 1.0 minute. Fluorescence measurements were performed at an excitation wavelength of 335 nm, monitoring dual emission at 445 nm (TA-CDs emission) and 545 nm (eosin emission). The ratiometric fluorescence intensity (F_{445}/F_{545}) was calculated and correlated with paraquat concentration for quantitative analysis.

2.6. Detection of paraquat in real samples

To assess the practical performance of the dual-emission ratiometric system, real-world samples including Nile River water and cabbage were analyzed. River water specimens were obtained from Ibrahimiya Canal (Assiut, Egypt) using cleaned polyethylene containers, subjected to membrane filtration (0.45 μm pore size) for particulate removal, and maintained at 4 °C prior to testing. Fresh cabbage was obtained from local markets in Assiut, Egypt, cleaned sequentially with municipal and deionized water, and allowed to dry naturally under ambient conditions. Sample extraction involved blending finely cut cabbage tissue (10 g) with acetonitrile (20 mL) in a high-speed homogenizer for three minutes. Following centrifugation (8000 rpm, 10 min), the liquid phase was isolated and concentrated to complete dryness using nitrogen gas. The dried extract was redissolved in deionized water (5 mL) and clarified through 0.22 μm filtration. Accuracy evaluation was performed by fortifying both processed water and cabbage matrices with paraquat standards at three concentration levels (5.0, 10.0, and 15.0 nM) prior to fluorescence measurement.

3. Results and discussion

3.1. Characterization of TA-CDs

Transmission electron microscopy (TEM) analysis revealed that the synthesized TA-CDs exhibited uniform dispersion with near-spherical morphology (Fig. 1A). Particle size distribution analysis showed carbon dots ranging from 2.7 to 6.8 nm in diameter, with a mean particle size of 5.4 nm, indicating successful formation of quantum-confined nanostructures. The narrow size distribution and excellent monodispersity demonstrate the effectiveness of the hydrothermal synthesis approach in producing homogeneous carbon dots suitable for consistent optical performance.

Raman spectroscopy was used to analyze the structural properties of the TA-CDs (Fig. 1B). The spectrum exhibited two prominent peaks: the D band at 1379 cm^{-1}, corresponding to disordered or defective carbon structures with sp^3 hybridization, and the G band at 1603 cm^{-1}, linked to the in-plane vibration of sp^2 hybridized carbon atoms in graphitic domains. The intensity ratio of G/D bands (I_G/I_D) was calculated to be 1.46, indicating a relatively high degree of graphitization with well-organized sp^2 carbon networks, which contributes to the favorable optical properties of the carbon dots.[41]

Fourier-transform infrared spectroscopy (FTIR) was performed to identify the surface functional groups of TA-CDs (Fig. 1C). The broad absorption band at 3434 cm^{-1} was assigned to O–H stretching vibrations from hydroxyl and carboxyl groups. The peak at 2922 cm^{-1} corresponded to aliphatic C–H stretching vibrations. Strong absorption bands at 1693 cm^{-1} and 1612 cm^{-1} were linked to C=O stretching of carboxylic acid/carbonyl groups and aromatic C=C stretching, respectively, originating from the polyphenolic structure of tannic acid precursor.[42] The peaks at 1434 cm^{-1} and 1320 cm^{-1} were associated with O–H bending and C–O stretching vibrations. Additional bands at 1235 cm^{-1} and 1021 cm^{-1} indicated C–O–C stretching vibrations from ether linkages and C–OH stretching, while the peak at 580 cm^{-1} corresponded to out-of-plane bending vibrations. These abundant oxygen-containing functional groups enhance the hydrophilicity and colloidal stability of TA-CDs in aqueous solution.[43]

X-ray photoelectron spectroscopy (XPS) was conducted to determine the elemental composition and chemical states of TA-CDs (Fig. 1D). The survey spectrum revealed two prominent peaks at 286.58 eV and 533.51 eV, corresponding to carbon (C 1s) and oxygen (O 1s), respectively, indicating that the carbon dots consist mainly of carbon and oxygen atoms originating from tannic acid. The high-resolution C 1s spectrum was resolved into three distinct peaks at 284.68 eV (C–C/C=C, sp^2-hybridized carbon), 285.66 eV (C–O associated with hydroxyl and epoxy groups), and 288.38 eV (C=O corresponding to carbonyl and carboxyl functionalities) (Fig. 1E).[44] The O 1s spectrum was resolved into three components at 531.26 eV (C=O in carbonyl groups), 532.37 eV (C–O in hydroxyl and ether groups), and 533.23 eV (O–C=O in carboxyl groups) (Fig. 1F).[45] The XPS analysis corroborates the FTIR results, confirming the presence of multiple oxygen-containing functional groups on
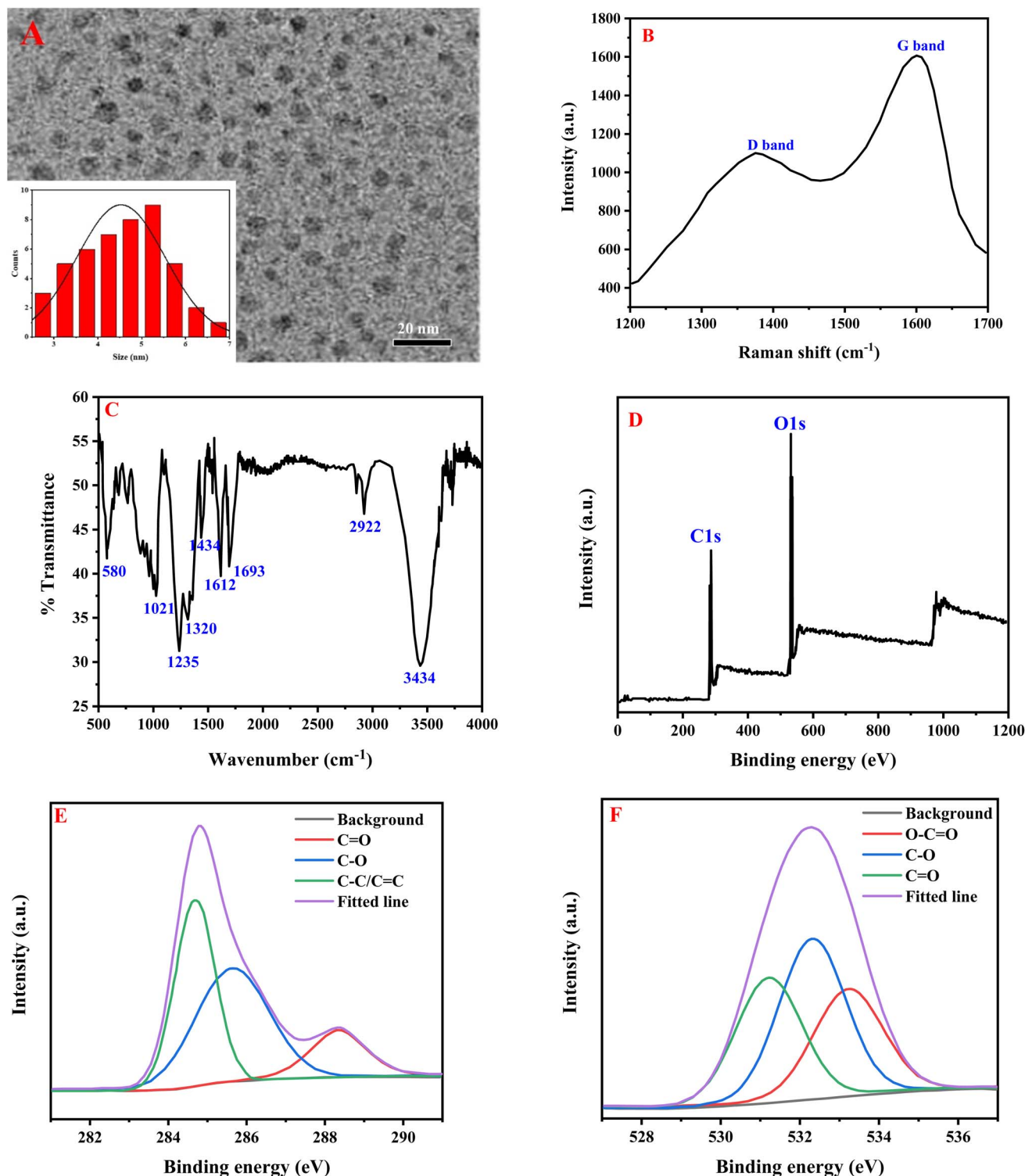
Fig. 1 (A) TEM image with inset particle-size histogram; (B) Raman spectrum; (C) FT-IR spectrum; (D) survey XPS spectrum; high-resolution XPS of (E) C 1s and (F) N 1s of TA-CDs.

the carbon dot surface, which are essential for their fluorescence properties and interaction with paraquat analyte.

The optical properties of TA-CDs were systematically investigated using UV-visible absorption and fluorescence spectroscopy. The UV-vis absorption spectrum exhibited two characteristic peaks at 213 nm and 275 nm, attributed to π–π^* transitions of aromatic C=C bonds and n–π^* transitions of C=O groups, respectively (Fig. 2A), consistent with the polyphenolic structure derived from tannic acid precursor.[46] Fluorescence analysis revealed optimal excitation at 335 nm with maximum emission at 445 nm, exhibiting bright blue fluorescence characteristic of carbon dots. The influence of excitation
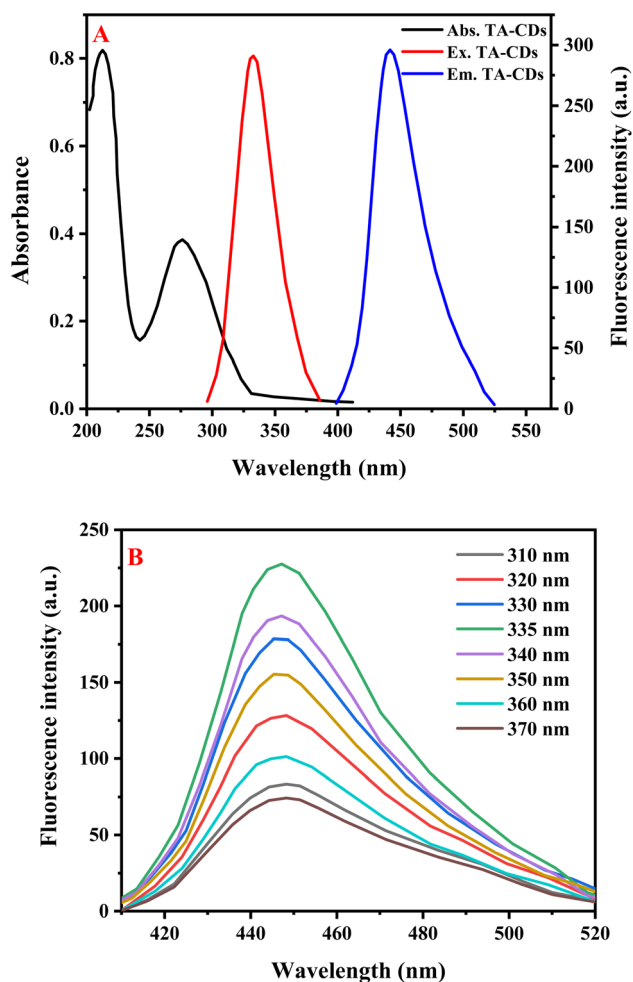
Fig. 2 (A) UV-vis absorption (black), excitation (red), and fluorescence emission (blue) spectra of 1.0 mg mL^{-1} of TA-CDs in phosphate buffer (50 mM, pH 8.0). (B) Emission spectra recorded at excitation wavelengths from 310 to 370 nm in 10 nm steps.

wavelength on emission characteristics was investigated across a spectral range of 310 to 370 nm (Fig. 2B), revealing that the emission peak position was maintained at 445 nm throughout this excitation window, although the fluorescence signal strength exhibited wavelength-dependent variations. This excitation-independent emission behavior indicates uniform surface states and homogeneous energy levels within the TA-CDs, contrasting with typical carbon dots that exhibit excitation-dependent emission due to heterogeneous surface chemistry.[47] The fluorescence quantum yield of TA-CDs was determined to be 17.23% using quinine sulfate in 0.1 M H$_2$SO$_4$ as a reference standard (quantum yield = 54%), indicating moderate fluorescence efficiency suitable for sensing applications.

3.2. Stability assessment of TA-CDs

The stability of TA-CDs under various environmental conditions was systematically evaluated to assess their suitability for practical analytical applications. pH stability studies revealed

that the fluorescence intensity remained relatively constant across a broad pH range from 3 to 8, indicating excellent resistance to acidic and near-neutral conditions (Fig. S1A). However, a fluorescence decrease was observed at pH values above 8, likely due to deprotonation of surface functional groups and potential aggregation under strong alkaline conditions, which may alter the electronic structure and surface states of the carbon dots.[48] Ionic strength tolerance was examined by varying NaCl concentration from 0.01 to 2.0 M (Fig. S1B), demonstrating that TA-CDs maintained stable fluorescence across this wide range, confirming minimal salt-induced aggregation and robust colloidal stability attributed to electrostatic and steric repulsion from abundant surface oxygen-containing groups. Photostability assessment under continuous UV irradiation (365 nm) showed that TA-CDs sustained approximately 400 minutes of exposure with negligible fluorescence decay (Fig. S1C), indicating exceptional resistance to photobleaching compared to conventional organic dyes. Temperature-dependent studies demonstrated stable fluorescence signals from 20 to 80 °C (Fig. S1D), suggesting that thermal effects do not significantly impact the carbon dot structure or surface states within this operational range. Collectively, these results confirm the robust stability of TA-CDs under diverse environmental conditions, making them highly suitable for reliable sensing applications in complex matrices.

3.3. Optimization of fluorescence detection

To achieve optimal analytical performance for paraquat detection, key experimental parameters affecting the dual-emission ratiometric response were systematically optimized. The effect of pH on the fluorescence ratio (F_{445}/F_{545}) was investigated over the range of 4 to 10 in the presence of a fixed paraquat concentration (Fig. S2A). The detection mechanism relies on electrostatic interactions between the positively charged paraquat cation and the negatively charged surfaces of both eosin and TA-CDs. At lower pH values (4–6), protonation of carboxyl and hydroxyl groups on TA-CDs and eosin reduces their negative charge density, weakening electrostatic attraction with paraquat and diminishing the ratiometric response. The fluorescence ratio increased with pH and reached maximum at pH 8, where optimal ionization states enable strong electrostatic binding: paraquat induces quenching of eosin fluorescence (545 nm) through charge transfer interactions, while simultaneously causing aggregation-induced fluorescence enhancement of TA-CDs (450 nm) via electrostatic cross-linking. At pH values above 8, excessive negative charge and potential structural changes in the carbon dots led to non-specific aggregation, reducing the analytical signal. Therefore, pH 8 was selected as optimal, providing maximum ratiometric response and physiological relevance for real sample analysis. The reaction time between paraquat and the dual-emission system was optimized from 0.5 to 15 minutes (Fig. S2B). The fluorescence ratio changed rapidly within the first minute, reaching equilibrium at approximately 1.0 minute due to fast electrostatic interactions, after which the signal remained stable for at least 15 minutes. Consequently, 1.0 minute was chosen as the optimal

incubation time, ensuring complete electrostatic binding while maintaining high sample throughput for practical applications.

3.4. Detection of paraquat using dual-emission ratiometric system

The analytical performance of the eosin/TA-CDs dual-emission system for paraquat detection was evaluated by monitoring fluorescence changes upon increasing paraquat concentration from 0 to 150 nM (Fig. 3A). Upon addition of paraquat, a distinct ratiometric response was observed: the TA-CDs emission at 445 nm progressively increased due to aggregation-induced fluorescence enhancement *via* electrostatic cross-linking of negatively charged carbon dots by positively charged paraquat cations, while eosin emission at 545 nm simultaneously decreased through electrostatic interaction-induced quenching. This opposite fluorescence behavior created a robust ratiometric signal (F_{445}/F_{545}) that exhibited excellent linearity over the concentration range of 5–150 nM with a strong correlation

coefficient ($R^2 = 0.9973$) and a regression equation of $F_{445}/F_{545} = 0.051 + 0.0104$ [paraquat] (Fig. 3B). The limit of detection was calculated as 2.11 nM based on 3σ/slope, where σ represents the standard deviation of ten blank measurements. The dual-emission ratiometric readout offers significant advantages over previously reported single-signal fluorescence methods (Table S1), providing built-in self-calibration that eliminates environmental interferences, improves measurement reliability, and simplifies the detection procedure.

The analytical performance of the proposed eosin/TA-CDs dual-emission ratiometric sensor was compared with previously reported fluorescent methods for paraquat detection (Table S1). The developed method exhibits a competitive limit of detection (2.11 nM) that surpasses many conventional fluorescent probes including squaraines (372 nM),[25] polymeric probes (11 000 nM),[26] pyramine (200 nM),[27] CdS quantum dots (38.9 nM),[28] and fluorescent ionic liquids (64.0 nM),[49] while being comparable to advanced nanomaterial-based sensors such as TGA CdTe/CdS NCs (3.5 nM),[29] GSH/β-CDs-AuNCs (4.7 nM),[50] and SiO$_2$@CdTe QDs@MIP (1.94 nM).[51] Although some methods such as BPNSs (0.70 nM),[24] calix[6]arene (0.12 nM),[52] and cucurbit[8]uril (0.24 nM)[53] achieve lower detection limits, the proposed method offers several distinct advantages: (1) dual-emission ratiometric readout provides built-in self-calibration that eliminates environmental interferences from instrumental fluctuations, sample turbidity, and matrix effects—a critical advantage over single-signal methods that are susceptible to false positives; (2) simultaneous applicability to both water and food matrices without requiring different protocols or modifications, whereas many reported methods are limited to specific sample types; (3) utilization of metal-free, low-toxicity carbon dots derived from biocompatible tannic acid precursor, avoiding the environmental and health concerns associated with cadmium-based quantum dots (CdS QDs, CdTe QDs);[28,29,51] (4) simple, one-step hydrothermal synthesis requiring no complex organic chemistry or expensive reagents, contrasting with elaborate syntheses needed for calixarenes,[52] cucurbiturils,[53] or molecularly imprinted polymers;[51] (5) rapid analysis (1 minute reaction time) with minimal sample pretreatment and straightforward operation suitable for on-site testing; and (6) cost-effective instrumentation using conventional fluorescence spectroscopy without requiring specialized detection systems. The practical linearity range (0.005–0.15 μM) adequately covers environmentally and agriculturally relevant concentrations, making this method highly suitable for routine monitoring of paraquat residues in food safety and environmental surveillance programs.

The proposed TA-CDs/eosin sensor outperforms similar dual-emission ratiometric systems through superior sensitivity (LOD 2.11 nM *vs.* 3.03–6.5 nM),[54,55] metal-free cost-effective design eliminating expensive copper/gold nanoclusters, and a unique dual opposite-response mechanism (aggregation-enhancement + quenching) providing greater signal dynamic range than single-quenching approaches. Critically, validation in real agricultural cabbage samples with time-resolved residue monitoring demonstrates practical food safety capability beyond laboratory-spiked samples typical of reported dual-emission methods.
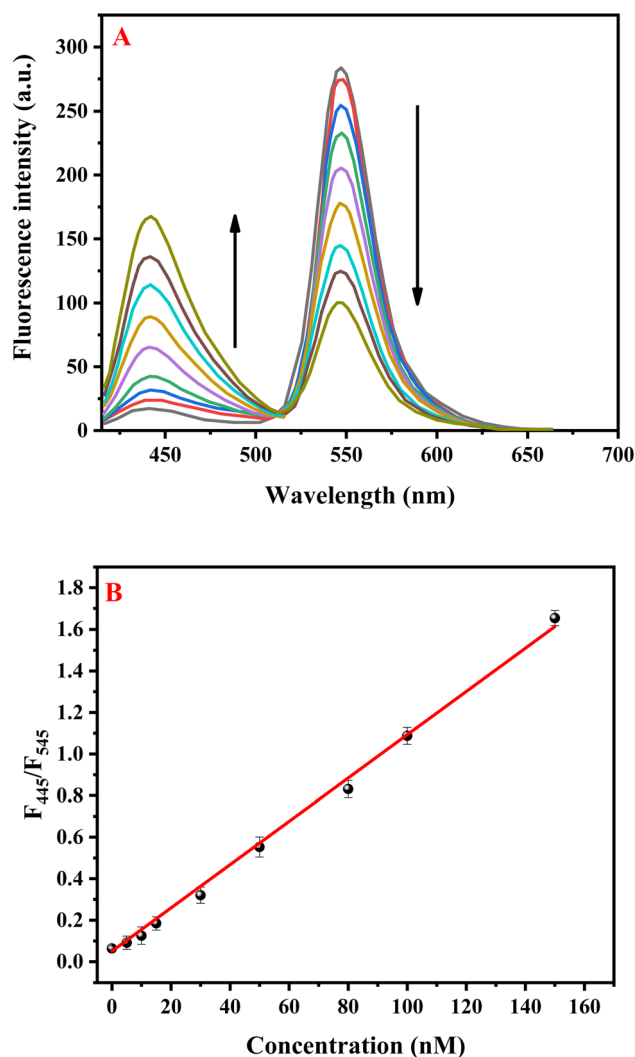

Fig. 3 (A) Fluorescence spectra of the eosin/TA-CDs system with paraquat from 0 to 150.0 nM in phosphate buffer (50 mM, pH 8.0). (B) Linear calibration of the intensity ratio F_{445}/F_{545} *versus* paraquat concentration (5.0–150.0 nM).

3.5. Selectivity evaluation

The selectivity of the dual-emission ratiometric sensor was systematically evaluated by measuring the fluorescence response to 50 nM paraquat in the presence of various potentially interfering species at ten-fold higher concentrations (500 nM) (Fig. 4). The tested interferents included various herbicides (diquat, diazinon, dichlorvos, glyphosate, atrazine, pendimethalin, fluroxypyr, propisochlor, quizalofop, tribenuron-methyl, acetochlor, metolachlor, and tebuconazole), common organic substances (humic acid, urea, and citric acid), monovalent cations (Na^+, K^+, NH_4^+), divalent cations (Ca^{2+}, Mg^{2+}, Fe^{2+}, Cu^{2+}, Zn^{2+}, Ni^{2+}, Pb^{2+}, Hg^{2+}), trivalent cations (Al^{3+}), and common anions (Cl^-, NO_3^-, SO_4^{2-}, HCO_3^-, PO_4^{3-}). The results demonstrated that none of these interferents caused significant changes in the fluorescence ratio (F_{445}/F_{545}), with deviations remaining below $\pm 5\%$ compared to paraquat alone, except for diquat which exhibited a response comparable to paraquat. Original fluorescence spectra of the eosin/TA-CDs system upon addition of various herbicides (Fig. S3) demonstrate selective ratiometric response exclusively to paraquat and diquat among all tested compounds, with both inducing simultaneous TA-CD emission enhancement at 445 nm and eosin quenching at 545 nm. The response to both paraquat and diquat is attributed to their shared structural feature: permanent dicationic quaternary nitrogen centers (N,N'-dimethyl-4,4'-bipyridinium for paraquat; ethylene-bridged bipyridinium for diquat) with delocalized positive charges capable of simultaneous electrostatic bridging between negatively charged TA-CDs and eosin. This selectivity mechanism was further validated through complementary characterization techniques. Zeta potential measurements (Fig. S4A) revealed significant increases (reduced negative charge) of TA-CDs only upon interaction with paraquat (-28.5 to -12.3 mV) and diquat (-28.5 to -5.7 mV), while other herbicides produced negligible changes, confirming that electrostatic interaction and subsequent aggregation occur specifically with dicationic species. TEM imaging of TA-CDs after interaction with an electrostatically inert herbicide such as diazinon (Fig. S4B) revealed maintained dispersion with individual particles averaging 6.8 nm, contrasting sharply with paraquat-induced cluster formation, thereby validating the aggregation-based fluorescence enhancement mechanism. Additionally, systematic evaluation of herbicide effects on eosin fluorescence (Fig. S5) demonstrated that only paraquat and diquat—both possessing permanent dicationic structures—induce significant eosin quenching at 545 nm, while other tested herbicides including weakly basic (atrazine) or neutral species (diazinon, glyphosate) produce negligible effects (<5%), confirming that the static quenching mechanism *via* electrostatic binding is specific to strongly dicationic herbicides. The exceptional dual-channel selectivity arises from the unique recognition mechanism requiring simultaneous fulfillment of two conditions: (1) the analyte must be a dication with appropriate charge density and molecular geometry to induce electrostatic aggregation of TA-CDs, causing fluorescence enhancement at 445 nm, and (2) it must simultaneously quench eosin emission at 545 nm through specific charge-transfer and electrostatic interactions. Diazinon and other tested pesticides, despite some being structurally similar organics, are predominantly neutral or monoanionic species lacking permanent positive charges, thus failing to trigger the electrostatic-driven dual response. Metal cations, despite their positive charges, do not induce the characteristic ratiometric response due to their inability to simultaneously bridge and aggregate carbon dots while quenching eosin through π–π or charge-transfer interactions. While the response to both paraquat and diquat represents a limitation for exclusive single-analyte detection, it can be viewed as an advantage for broader quaternary bipyridinium herbicide monitoring, as these compounds are rarely co-applied and both require environmental and food safety surveillance. This dual-response requirement acts as a molecular logic gate, ensuring high selectivity even in complex environmental and agricultural matrices.
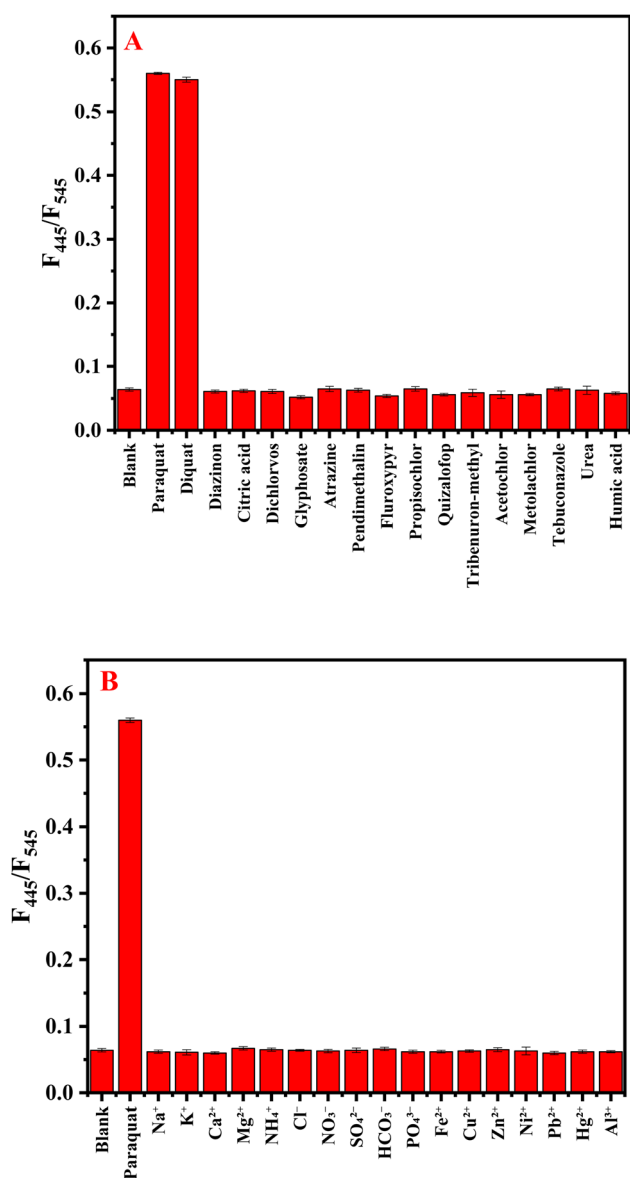

Fig. 4 Response of the eosin/TA-CDs system to different (A) structurally related herbicides, common organic substances, (B) metal ions and anions.

3.6. Mechanism of detection

To elucidate the fluorescence enhancement mechanism of TA-CDs upon paraquat addition, spectral overlap analysis was performed between the UV-vis absorption spectrum of paraquat and both the excitation and emission spectra of TA-CDs. The results revealed no significant spectral overlap between paraquat absorption and either the excitation spectrum (maximum at 335 nm) or emission spectrum (maximum at 445 nm) of TA-CDs (Fig. 5A). This absence of spectral overlap conclusively rules out inner filter effect (IFE) and Förster resonance energy transfer (FRET) as potential mechanisms for the observed fluorescence changes.[56] Since neither mechanism
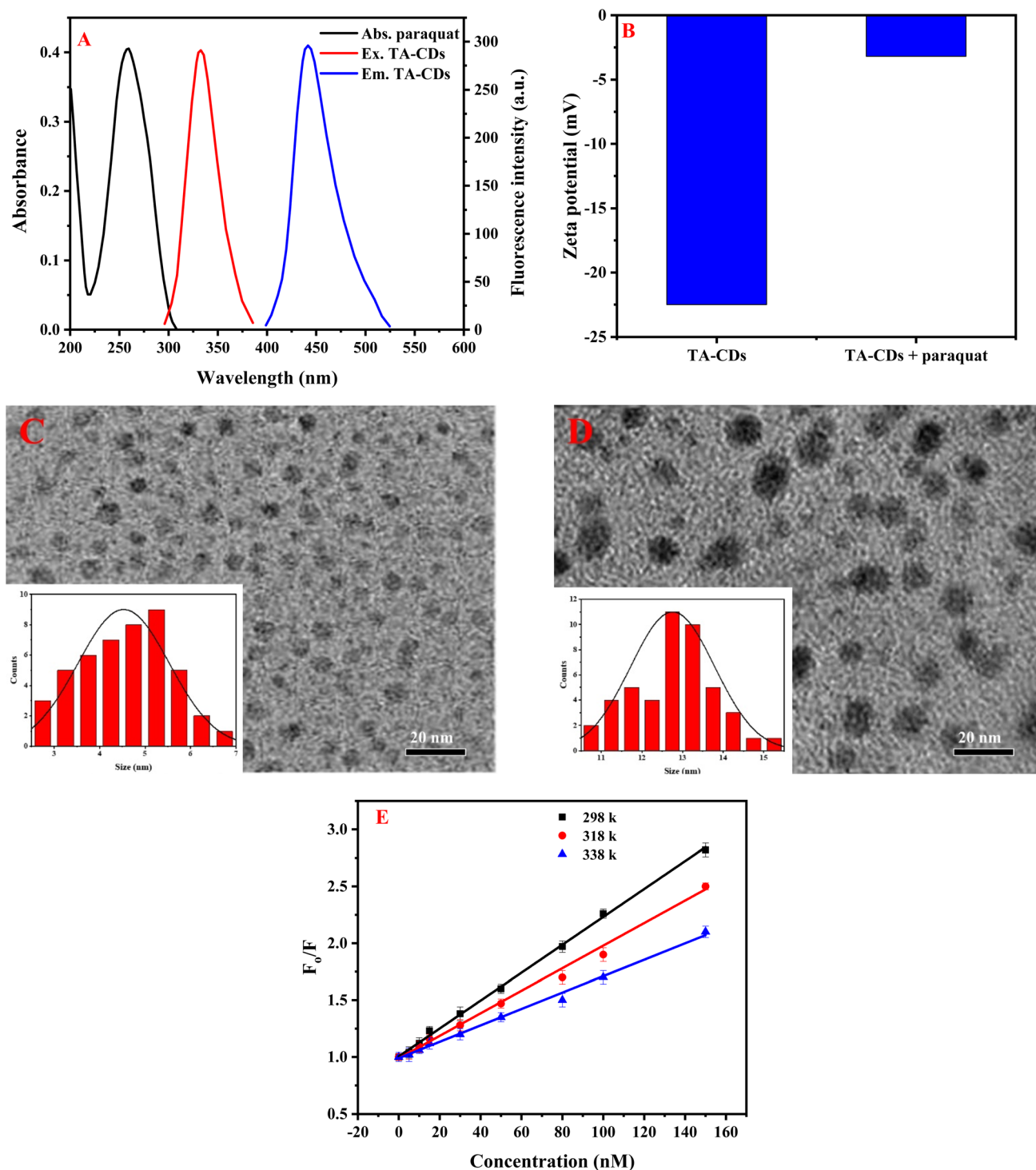

Fig. 5 (A) Spectral overlay of UV-vis spectrum of paraquat, excitation and emission spectra of TA-CDs, (B) zeta potential of TA-CDs before and after addition of paraquat, (C) and (D) TEM images of TA-CDs before and after addition of paraquat, (E) Stern–Volmer plot at different temperatures.

applies here, the fluorescence enhancement observed upon paraquat addition must arise from aggregation-induced emission (AIE) or aggregation-enhanced emission (AEE) phenomena,[57] where restriction of intramolecular motions and changes in the electronic environment upon nanoparticle assembly lead to increased radiative decay pathways (Scheme 1).

Surface charge characterization was performed using zeta potential measurements to confirm electrostatic interactions between paraquat and TA-CDs (Fig. 5B). The pristine TA-CDs exhibited a highly negative zeta potential of approximately −22.5 mV at pH 8, attributed to the abundant carboxyl (–COO⁻) and hydroxyl (–O⁻) groups on their surface as confirmed by FTIR and XPS analyses. Upon addition of paraquat (concentration ratio of 1 : 1), the zeta potential shifted significantly toward less negative values (approximately −3.2 mV), indicating neutralization of the surface negative charges through electrostatic binding with the dicationic paraquat molecules. This substantial reduction in surface charge confirms strong electrostatic interactions and provides direct evidence for the proposed mechanism wherein positively charged paraquat cations bridge between multiple negatively charged TA-CDs, reducing electrostatic repulsion and facilitating aggregation. The residual negative charge after paraquat addition suggests incomplete surface neutralization, maintaining colloidal stability while enabling controlled aggregation that enhances fluorescence.

Transmission electron microscopy was employed to directly visualize the morphological changes of TA-CDs upon paraquat addition (Fig. 5C and D). TEM images of pristine TA-CDs showed well-dispersed, individual nanoparticles with an average diameter of 5.4 nm, consistent with the initial characterization. In contrast, TEM images obtained after addition of paraquat (10 nM) revealed distinct aggregation behavior, with carbon dots assembling into larger clusters with apparent diameters ranging from 10 to 16 nm. The aggregated structures maintained relatively uniform size distribution, suggesting controlled assembly rather than random precipitation. Importantly, the aggregation process is reversible upon dilution or addition of competing anions, indicating non-covalent electrostatic interactions as the driving force. These morphological changes provide direct visual evidence supporting the aggregation-induced fluorescence enhancement mechanism: the dicationic paraquat molecules act as electrostatic cross-linkers between negatively charged TA-CDs, bringing multiple nanoparticles into close proximity. This aggregation restricts intramolecular rotations and vibrations of surface functional groups, reduces non-radiative decay pathways,[58] and potentially creates new emissive states through inter-particle electronic coupling, collectively resulting in the observed fluorescence enhancement at 445 nm.

To elucidate the quenching mechanism responsible for the decreased eosin fluorescence upon paraquat addition, Stern–Volmer analysis was performed at different temperatures. Eosin fluorescence can be quenched through multiple pathways including ion-pairing, dynamic (collisional) quenching, static quenching (ground–state complex formation), and FRET. The fluorescence quenching data were analyzed using the Stern–Volmer equation: $F_0/F = 1 + K_{sv}[C]$, where F_0 and F represent the fluorescence intensities of eosin in the absence and presence of
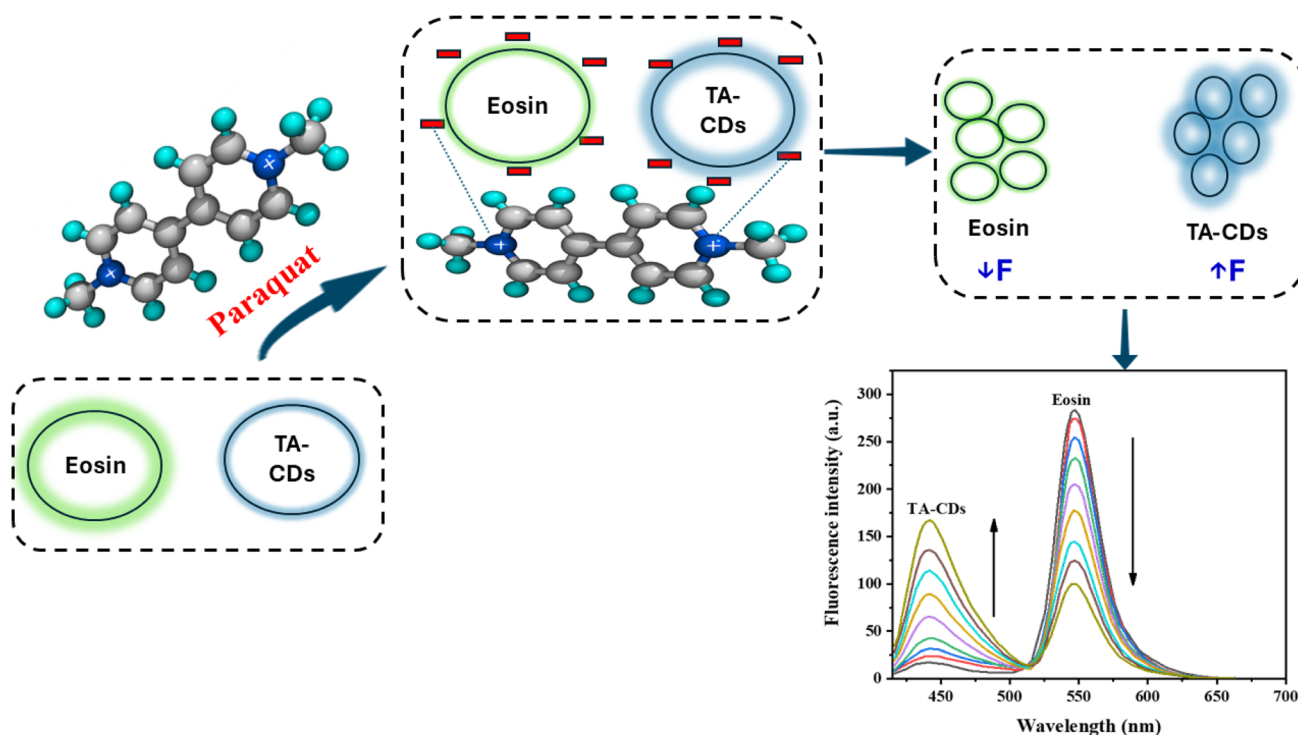
Scheme 1 Summary of detection mechanism of paraquat using Eosin/TA-CDs system.

Table 1 Results of the analysis of paraquat in real samples ($n = 3$)

Sample	Proposed method				Reported method		
	Added (nM)	Found (nM)	Recovery%	RSD%	Found (nM)	Recovery%	RSD%
Cabbage	5.0	4.98	99.6	3.51	4.78	95.6	4.12
	10.0	9.69	96.9	4.28	9.91	99.1	3.31
	15.0	14.79	98.6	3.38	14.53	96.9	3.64
River water	5.0	4.82	96.4	3.02	4.82	96.4	3.81
	10.0	9.82	98.2	2.82	10.02	100.2	2.99
	15.0	14.72	98.1	3.36	14.66	97.7	3.61

paraquat, respectively, K_{sv} is the Stern–Volmer quenching constant, and $[C]$ is the paraquat concentration (Fig. 5E).[59] Temperature-dependent studies were conducted at 298 K, 318 K, and 338 K, revealing that the Stern–Volmer quenching constant (K_{sv}) decreased systematically with increasing temperature (K_{sv} values: 0.0123 nM^{-1} at 298 K, 0.0099 nM^{-1} at 308 K, and 0.0072 nM^{-1} at 318 K). This inverse temperature dependence is characteristic of static quenching mechanisms, wherein ground-state complex formation between eosin and paraquat occurs, and elevated temperatures destabilize the complex, reducing quenching efficiency. In contrast, dynamic (collisional) quenching exhibits increased K_{sv} values at higher temperatures due to enhanced diffusion rates and collision frequencies. The observed behavior indicates that static quenching dominates the eosin-paraquat interaction, involving electrostatic binding between the negatively charged xanthene moiety of eosin (containing carboxylate and brominated aromatic groups) and the positively charged bipyridinium structure of paraquat, forming a non-fluorescent ground-state complex. This electrostatic complex formation not only quenches eosin fluorescence at 545 nm but also serves as the complementary signal change in the ratiometric detection system, working synergistically with the aggregation-enhanced fluorescence of TA-CDs at 445 nm to provide a robust dual-response sensor for paraquat.

3.7. Application of the proposed method to real samples

The practical applicability of the dual-emission ratiometric sensor was evaluated using real environmental and food matrices, including Nile River water and cabbage samples. Recovery studies were conducted by spiking three different concentrations of paraquat (5.0, 10.0, and 15.0 nM) into both pre-analyzed matrices. For Nile River water samples, excellent recovery percentages ranging from 96.4% to 98.2% were obtained with relative standard deviations (RSD) below 3.36% ($n = 3$), demonstrating high accuracy and precision even in the presence of natural organic matter, dissolved ions, and other matrix components (Table 1). Similarly, cabbage extracts yielded satisfactory recoveries between 96.9% and 99.6% with RSD values less than 4.28%, confirming the method's robustness in complex food matrices containing pigments, proteins, and other interfering substances. To validate the reliability of the proposed method, parallel analyses were performed using a previously reported chromatographic method,[10] and the

results were subjected to statistical comparison using a paired t-test at the 95% confidence level. The analysis revealed no statistically significant difference between the two methods for both Nile River water samples ($t_{calculated} = 1.85 < t_{critical} = 4.30$, $p > 0.05$) and cabbage extracts ($t_{calculated} = 2.21 < t_{critical} = 4.30$, $p > 0.05$), confirming that the dual-emission ratiometric sensor provides comparable accuracy to established chromatographic techniques across different sample matrices while offering advantages of simplified sample preparation, reduced analysis time, and lower instrumentation costs.

To demonstrate real-world applicability, the developed method was applied to analyze paraquat residues in cabbage leaves collected from agricultural fields where the herbicide had been applied according to standard farming practices. Fresh cabbage samples were obtained from Assiut farms at different time intervals post-application (1, 3, 7, and 14 days after spraying). Following the extraction procedure described in section 2.6, paraquat concentrations were determined to be 98.65, 77.65, 37.56, and 12.35 µg g^{-1} at 1, 3, 7, and 14 days post-application, respectively, showing a gradual decline over time due to natural degradation and washing effects. Notably, samples collected 1 and 3 days after application exhibited paraquat levels exceeding the maximum residue limit (MRL) of 0.05 mg kg^{-1} (50 µg g^{-1}) established by international food safety regulations (Codex Alimentarius and EU regulation), while samples collected at 7 and 14 days showed concentrations below the MRL threshold. These findings highlight the importance of adhering to pre-harvest intervals and demonstrate that the proposed ratiometric sensor can effectively monitor compliance with food safety standards. The method's ability to rapidly detect paraquat residues in real agricultural products without complex sample pretreatment positions it as a valuable tool for routine food safety monitoring, protecting consumer health, and ensuring regulatory compliance in agricultural supply chains.

4. Conclusion

This work established a novel dual-emission ratiometric fluorescent sensor for paraquat detection by combining tannic acid-derived carbon dots and eosin as complementary optical reporters. The dicationic paraquat simultaneously induces aggregation-enhanced fluorescence of TA-CDs and static quenching of eosin, generating a self-calibrated ratiometric signal resistant to matrix interferences. Comprehensive

characterization and mechanistic validation through spectral analysis, zeta potential, and electron microscopy confirmed the dual-recognition mechanism involving electrostatic cross-linking and ground–state complex formation. The sensor demonstrated excellent sensitivity, wide linearity, and exceptional selectivity due to the stringent requirement for simultaneous dual-response generation. Successful application to environmental water and food matrices with high recovery and validated accuracy against chromatographic methods confirms practical reliability. Real-world testing on agricultural produce demonstrated capability to track pesticide degradation and assess regulatory compliance. This biocompatible, metal-free platform offers rapid analysis, simplified sample preparation, and cost-effectiveness, addressing critical needs in food safety surveillance. The bioorthogonal recognition strategy established here can be extended to other ionic pesticides and environmental contaminants, contributing to safer agricultural practices and enhanced public health protection in the global food supply chain.

Conflicts of interest

There are no conflicts to declare.

Data availability

Data will be made available upon request.

Supplementary information is available. See DOI: https://doi.org/10.1039/d5ra07809a.

Acknowledgements

References

1 D. Gunnell, M. Eddleston, M. R. Phillips and F. Konradsen, *BMC Public Health*, 2007, **7**, 357.

2 C. A. Sukumar, V. Shanbhag and A. B. Shastry, *Indian J. Crit. Care Med.*, 2019, **23**, S263–s266.

3 C. Vaccari, R. El Dib, H. Gomaa, L. C. Lopes and J. L. de Camargo, *J. Toxicol. Environ. Health, Part B*, 2019, **22**, 172–202.

4 D. L. Weed, *Neurotoxicology*, 2021, **86**, 180–184.

5 M. Asaduzzaman, S. Roy, N. Das Pew, A. D. Roy, S. Kibria, R. K. Roy, M. M. J. Alam and S. R. Chakraborty, *Toxicol Rep*, 2023, **11**, 350–354.

6 R. J. Dinis-Oliveira, J. A. Duarte, A. Sánchez-Navarro, F. Remião, M. L. Bastos and F. Carvalho, *Crit. Rev. Toxicol.*, 2008, **38**, 13–71.

7 L. Gao, H. Yuan, E. Xu and J. Liu, *Sci. Rep.*, 2020, **10**, 1790.

8 Z. Li and P. Fantke, *Pest Manage. Sci.*, 2023, **79**, 748–759.

9 V. Y. Taguchi, S. W. D. Jenkins, P. W. Crozier and D. T. Wang, *J. Am. Soc. Mass Spectrom.*, 1998, **9**, 830–839.

10 I. R. Pizzutti, G. M. E. Vela, A. de Kok, J. M. Scholten, J. V. Dias, C. D. Cardoso, G. Concenço and R. Vivian, *Food Chem.*, 2016, **209**, 248–255.

11 T. Zou, P. He, J. Cao and Z. Li, *J. Chromatogr. Sci.*, 2015, **53**, 204–209.

12 W. Zheng, R. Su, G. Yu, L. Liu and F. Yan, *Nanomaterials*, 2022, **12**, 3632.

13 Q. Wu, H. Tao, Y. Wu, X. Wang, Q. Shi and D. Xiang, *Foods*, 2022, **11**, 2405.

14 S. Thimoonnee, K. Somnet, P. Ngaosri, S. Chairam, C. Karuwan, W. Kamsong, A. Tuantranont and M. Amatatongchai, *Anal. Methods*, 2022, **14**, 820–833.

15 T. Y. Wang, Y. T. Lee, H. Y. Chen, C. H. Ko, C. T. Hong, J. W. Wen, T. H. Yen and C. M. Cheng, *Diagnostics*, 2020, 11.

16 N. koohzadi and Z. Rezayati Zad, *Adv. J. Chem., Sect. B*, 2021, **3**, 311–322.

17 D. Y. Lin, C. Y. Yu, C. A. Ku and C. K. Chung, *Micromachines*, 2023, **14**, 1343.

18 Y.-Y. Zhang, L.-H. Li, Y. Wang, H. Wang, Z.-L. Xu, Y.-X. Tian, Y.-M. Sun, J.-Y. Yang and Y.-D. Shen, *Biosens. Bioelectron.*, 2022, **205**, 114089.

19 A. Helal, M. Naeem, M. E. Arafat and M. M. Rahman, *Mater. Res. Bull.*, 2022, **146**, 111604.

20 P. Wang, H. Li, W. Jia, Y. Chen and R. Gerhards, *Sensors*, 2018, **18**, 3771.

21 A. Helal, M. Naeem, M. Fettouhi and M. H. Zahir, *Molecules*, 2021, **26**, 5773.

22 A. Helal, M. Y. Khan, A. Khan, M. Usman and M. H. Zahir, *Int. J. Mol. Sci.*, 2023, **24**, 13045.

23 J. Zhang, H. Hu, J. Wang, K. Lu, Y. Zhou, L. Zhao and J. Peng, *Anal. Chim. Acta*, 2024, **1298**, 342380.

24 L. Wang, S. A. Haruna, W. Ahmad, J. Wu, Q. Chen and Q. Ouyang, *Food Chem.*, 2022, **388**, 132950.

25 J. Tu, L. Xiao, Y. Jiang, Q. He, S. Sun and Y. Xu, *Sens. Actuators, B*, 2015, **215**, 382–387.

26 N. F. Suhendra and H.-i. Lee, *J. Hazard. Mater.*, 2025, **494**, 138513.

27 Z. Zhao, F. Zhang and Z. Zhang, *Spectrochim. Acta, Part A*, 2018, **199**, 96–101.

28 H. Li, J. Liu and X. Yang, *Anal. Sci.*, 2015, **31**, 1011–1017.

29 Z. Pourghobadi, H. Makanali and H. Zare, *J. Fluoresc.*, 2021, **31**, 559–567.

30 F. A. M. Abdel-aal, A. M. Mahmoud, A. H. Rageh, M. R. Elmasry, Y. A. B. Jardan, M. M. El-Wekil and A. B. H. Ali, *Talanta Open*, 2025, **11**, 100438.

31 Y. A. B. Jardan, M. M. El-Wekil, A. M. Mostafa, J. Barker and A. B. H. Ali, *Microchem. J.*, 2025, **209**, 112789.

32 Y. A. Bin Jardan, A. M. Mostafa, J. Barker, A. B. H. Ali and M. M. El-Wekil, *Anal. Methods*, 2025, **17**, 3007–3016.

33 S. T. Alsharif, A. M. Mahmoud, M. M. El-Wekil and A. B. H. Ali, *Microchem. J.*, 2025, **208**, 112618.

34 A. M. Alaseem, K. Alhazzani, A. Z. Alanazi, S. M. Alsanad, O. A. Alkhamees, G. Alasiri, M. M. El-Wekil and A.-M. B. H. Ali, *Microchem. J.*, 2024, **207**, 111887.

35 J. Hu, Y. Sun, A. A. Aryee, L. Qu, K. Zhang and Z. Li, *Anal. Chim. Acta*, 2022, **1209**, 338885.

36 H. Man, M. Chaima, X. Wang, L. Xiu, L. Yang and J. Huang, *Arabian J. Sci. Eng.*, 2023, **48**, 8315–8324.

37 S. Wahyudi, A. Bahtiar, C. Panatarani, Anas and Risdiana, *Sens. Biosens. Res.*, 2023, **41**, 100576.

38 C. Liu, F. Ye and Y. Fu, *Talanta*, 2026, **296**, 128445.

39 A. Z. Alanazi, K. Alhazzani, H. Ibrahim, A. B. H. Ali, M. Darweesh, R. Y. Shahin and M. M. El-Wekil, *Microchem. J.*, 2024, **206**, 111625.

40 Z. X. Liu, Z. L. Wu, M. X. Gao, H. Liu and C. Z. Huang, *Chem. Commun.*, 2016, **52**, 2063–2066.

41 Z. Li, L. Deng, I. A. Kinloch and R. J. Young, *Prog. Mater. Sci.*, 2023, **135**, 101089.

42 O. Zaca-Moran, F. Díaz-Monge, A. Rodríguez-Juárez, C. L. Gómez-Muñoz, P. Zaca-Moran, O. Secundino-Sánchez and J. Díaz-Reyes, *Results Chem.*, 2024, **11**, 101788.

43 W. Fawaz, J. Hasian and I. Alghoraibi, *Sci. Rep.*, 2023, **13**, 18641.

44 H. Lin, J. Huang and L. Ding, *J. Nanomater.*, 2019, **2019**, 5037243.

45 M. Shao, Q. Yu, N. Jing, Y. Cheng, D. Wang, Y.-D. Wang and J.-H. Xu, *Lab Chip*, 2019, **19**, 3974–3978.

46 D. Ozyurt, M. A. Kobaisi, R. K. Hocking and B. Fox, *Carbon Trends*, 2023, **12**, 100276.

47 S. E. Elugoke, G. E. Uwaya, T. W. Quadri and E. E. Ebenso, in *Carbon Dots: Recent Developments and Future Perspectives*, American Chemical Society, 2024, vol. 1465, ch. 1, pp. 3–42.

48 Y. Z. Yang, N. Xiao, S. G. Liu, L. Han, N. B. Li and H. Q. Luo, *Mater. Sci. Eng. C*, 2020, **108**, 110401.

49 S. Che, X. Peng, Y. Zhuge, X. Chen, C. Zhou, H. Fu and Y. She, *J. Agric. Food Chem.*, 2022, **70**, 15390–15400.

50 H.-X. Ren, M.-X. Mao, M. Li, C.-Z. Zhang, C.-F. Peng, J.-G. Xu and X.-L. Wei, *Foods*, 2021, **10**, 1178.

51 J. Sun, C. Chen, Y. Zhang and X. Sun, *Luminescence*, 2021, **36**, 345–352.

52 E. Vasca, F. Siano and T. Caruso, *Sensors*, 2023, **23**, 1120.

53 S. Sun, F. Li, F. Liu, J. Wang and X. Peng, *Sci. Rep.*, 2014, **4**, 3570.

54 L. Chen, J. Lu, M. Luo, H. Yu, X. Chen, J. Deng, X. Hou, E. Hao, J. Wei and P. Li, *Food Chem.*, 2022, **379**, 132139.

55 S. Gong, L. Ma, F. Nie, M. Luo, S. Wu, T. Wang, Y. Yang, D. Chen, J. Wei and P. Li, *Talanta*, 2025, **286**, 127429.

56 S. Chen, Y.-L. Yu and J.-H. Wang, *Anal. Chim. Acta*, 2018, **999**, 13–26.

57 Y. Hong, J. W. Y. Lam and B. Z. Tang, *Chem. Commun.*, 2009, 4332–4353, DOI: **10.1039/B904665H**.

58 A. W. Kohn, Z. Lin and T. Van Voorhis, *J. Phys. Chem. C*, 2019, **123**, 15394–15402.

59 R. N. Motz, A. C. Sun, D. Lehnherr and S. Ruccolo, *ACS Org. Inorg. Au*, 2023, **3**, 266–273.